

Stabilizing an optical cavity containing a bulk diamond crystal at millikelvin temperatures in a cryogen-free dilution refrigerator

Tatsuki Hamamoto,^{1, a)} Amit Bhunia,^{2, a)} Hiroki Takahashi,¹ and Yuimaru Kubo²

¹⁾*Experimental Quantum Information Physics Unit, Okinawa Institute of Science and Technology Graduate University, Onna, Okinawa 904-0495, Japan*

²⁾*The Science and Technology Group, Okinawa Institute of Science and Technology Graduate University, Onna, Okinawa 904-0495, Japan*

(*Electronic mail: yuimaru.kubo@oist.jp)

(Dated: 3 February 2025)

We successfully stabilized a Fabry-Pérot optical cavity incorporating a bulk diamond crystal at millikelvin temperatures in a cryogen-free dilution refrigerator with the pulse-tube cryocooler running. In stark contrast to previous demonstrations where lasers were locked to the cavities, our setup locks the cavity to a laser. Our measurements of cavity length fluctuation suggest that the setup could stabilize a cavity up to a finesse of 1.2×10^4 without the diamond and 5.8×10^3 with the diamond crystal. The finesse with a diamond crystal of approximately 90 is primarily limited by the absorption loss inside the diamond.

I. INTRODUCTION

Optical cavities have diverse applications across various fields. They are critical in enhancing the stability and precision of lasers,¹ which is vital in optical communications. In metrology, they are used for highly accurate measurements, essential in both scientific research² and industrial applications. In quantum technology, optical cavities facilitate the control and manipulation of quantum states in the framework of cavity quantum electrodynamics (cavity-QED).^{3,4} Additionally, they will play an essential role in quantum network nodes that achieve quantum communication and/or distributed quantum computing.^{5,6} Apart from traditional applications, optical cavities operating at cryogenic temperatures, typically around 4 K, are also essential for a variety of quantum technologies such as a single photon source,^{7,8} ion trap,⁹ optomechanics,^{10,11} microwave-millimeter wave converter¹² or a gravitational wave detector.¹³

Traditionally, the optical cavities in such high-demand applications have been realized on stabilized optical tables to ensure the necessary mechanical stability and isolation from environmental vibrations at room temperature. Besides, the last two decades have witnessed significant advancements in microwave quantum devices operating at millikelvin temperatures in dilution refrigerators, paving the way for microwave-optical hybrid applications, such as quantum transducers.^{14–23} These devices bidirectionally convert optical and microwave photons, which is crucial for reliable quantum networks.^{6,24–26} Locking an optical cavity resonance frequency to the laser frequency is vital for photon indistinguishability in these applications. However, stabilizing an optical cavity length within the commonly used ‘cryogen-free’ dilution refrigerators poses significant challenges due to considerable mechanical vibrations from the pulse-tube cryocoolers.^{27–29}

One way to mitigate the cryocooler’s vibrations is to integrate optical cavities and peripheral components into a chip or device,^{30–34} to which optical signals transmit through optical fibers from room temperature to the device at the mixing

chamber stage. In such setups, the fibers and devices vibrate in a common mode, which effectively mitigates the vibration issue. However, this approach comes at the cost of losing the fast tunability of the cavity resonance frequency, which, in turn, requires the dynamical laser frequency tuning, as it must be *locked to the cavity* under such circumstances. Moreover, it introduces the technical challenge of achieving precise *in-situ* alignment to match the modes between the fibers’ output (or input) and the devices’ input (or output), which is further complicated by thermal drifts.

Apart from the challenges associated with integrating optical cavities in dilution refrigerators, impurity spins in diamond crystals have emerged as a promising resource for various quantum technology applications, including quantum sensing,^{35,36} microwave quantum memory,^{37–39} and stable photon sources.^{40–42} These spins are also potential candidates for spin-based microwave-optical photon transducers, which must be placed inside a dilution refrigerator. Additionally, the spin ensemble need to be coupled to a stabilized optical cavity for effective operation.^{22,23,43–47}

In this work, we mitigate the vibration issue by ensuring that the optical cavity, mounted at the coldest temperature stage, and the incoming optical beams share common mechanical modes, achieved through an optical breadboard installed on top. Using this setup, we reproducibly locked an *optical cavity to the laser* at approximately 15 mK. Our goal is to realize efficient microwave-optical photon quantum transduction^{22,23,34,43} using an ensemble of impurity spins in diamond crystals. As a first step, we incorporated a bulk diamond crystal into the optical cavity and successfully locked it.

Consequently, we achieved a root mean square (rms) cavity length fluctuation of approximately tens of pm during locking. This measured cavity length fluctuation indicates that the cavity can readily support an effective finesse of 1.2×10^4 (without diamond) and 5.8×10^3 (with a diamond crystal).

This paper is organized as follows: In Section II, we discuss the vibrations of our custom dilution refrigerator setup. Absolute and relative vibrations are measured and presented in Subsections II A and II B, respectively. In Section III, we describe the optical cavity device and measurement setup in Subsection III A and present the results of cavity stabilization,

^{a)}These two authors contributed equally

both with and without a diamond crystal, detailed in Subsections III B and III C, respectively. We also investigate the loss mechanism of diamond-integrated cavity in Subsection III D, the temperature-dependent effects in Subsection III E and analyze the vibration spectra in Subsection III F.

II. MECHANICAL VIBRATION OF A CRYOGEN-FREE DILUTION REFRIGERATOR

A. Absolute Vibration Measurement

First, we characterized the ‘absolute’ vibrations at the mixing chamber (MXC) stage inside a cryogen-free dilution refrigerator (Bluefors, LD-400). Figure 1(a) shows the schematic setup of the fridge. An optical breadboard is mounted on a 70mm-thick aluminum plate, which also supports the refrigerator’s main body. This plate is equipped with an active damping (AD) system to minimize the absolute vibrations primarily caused by the pulse-tube cryocooler (PT). We measured the absolute vibration levels on the MXC stage using a vibration sensor (Table Stable, VA-2C) under three conditions at room temperature: 1) PT on with AD off, 2) PT on with AD on, and 3) PT off with AD on.

The results are presented in Fig. 1(b), showing absolute vibration levels in root mean square (rms) of approximately $1.2\ \mu\text{m}$ (AD on) and $2.8\ \mu\text{m}$ (AD off). The values are an order of magnitude improvement compared to the value reported in Ref. 27 (indicated as “Hex std”) for a standard configuration of cryogen-free dilution refrigerator similar to ours. However, this value remains one to two orders of magnitude larger than those achieved in systems equipped with vibration isolation options (indicated as “Hex UQT” in Ref. 27), where the PT cold head and top flange are isolated via an edge-welded bellows, which is not present in our system.

B. Relative Vibration Measurement

To further mitigate vibrations, optical beam alignment was implemented on the top breadboard. This configuration was designed to synchronize the optical cavity device on the MXC plate with the fridge’s absolute vibrations in a common mode. Consequently, only the ‘relative’ vibrations prove to be significant. The relative vertical vibration was evaluated by measuring the interference between the reflected laser beam from the optical cavity’s input mirror and the local oscillator (LO), as depicted in Fig. 2(a). In this setup, a continuous wave Ti:Sapphire laser (M-squared, SolsTiS) with a wavelength of 737 nm was used (see Appendix B 3 for more details). To ensure the laser did not enter the cavity, we introduced a significant misalignment with respect to the cavity mode.

Figure 2(b) shows the relative vibration measurements at 15 mK under the conditions PT on AD off, PT on AD on, and PT off AD on. With PT on, the relative vibration amplitudes are approximately 5.6 nm in rms at millikelvin temperatures, which is three orders of magnitude less than the absolute vibration measurements, demonstrating effective vibration mitigation achieved using the optical breadboard on top of the fridge. Remarkably, in stark contrast to the absolute vibrations, no significant differences were observed between the

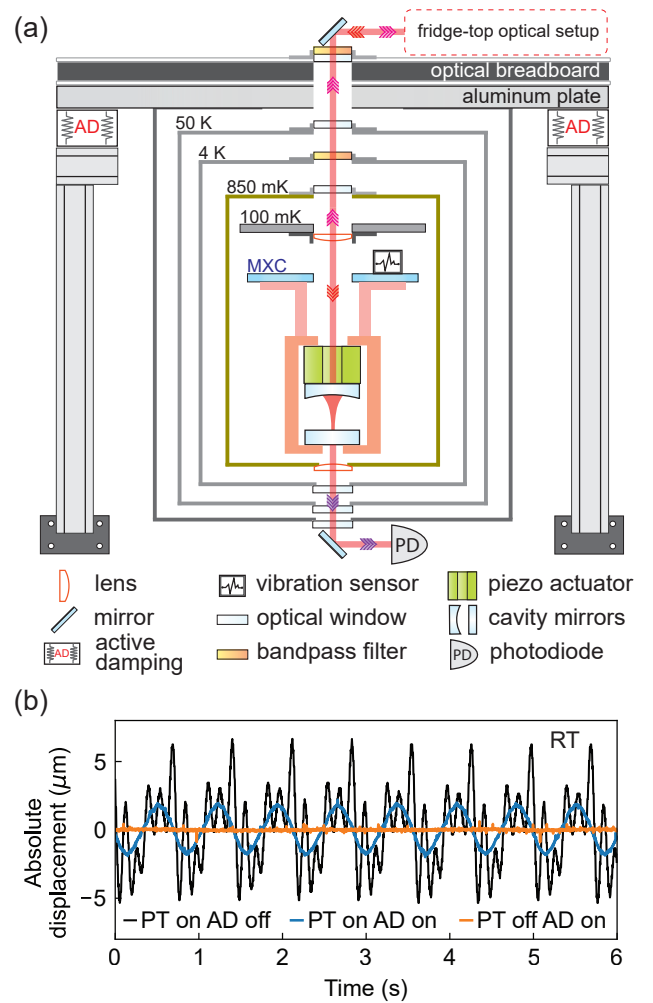


FIG. 1. The custom dilution refrigerator setup and vibration measurement. (a) Schematic of the custom dilution refrigerator. An active damping (AD) system supports an aluminum plate, on which both an optical breadboard and the main body of the refrigerator are mounted, suppressing the common-mode vibrations. A laser beam is directed inside via a 45-degree mirror. Different colored arrows indicate the propagation directions of the input, reflected, and transmitted light. The cavity is thermalized to the mixing chamber (MXC) plate through a cylindrical copper shroud. (b) Absolute vibrations measured on the MXC plate with a vibration sensor under three conditions: PT on with AD off, PT on with AD on, and PT off with AD on.

active damping (AD) on and off. Additionally, the measured vibration amplitudes are nearly identical to those measured at 4K without helium mixture circulation (see Fig.11 in Appendix C 1), suggesting the absence of detrimental vibrations from the turbo pump used during dilution refrigerator operations.

To assess the spectral response of the relative vibrations, we plot the amplitude spectral density (ASD) in Fig. 2(c), derived from the fast Fourier transform (FFT) of the data in Fig. 2(b). The spectra remain around $\sim 0.1\ \text{nmHz}^{-1/2}$ up to approximately 100 Hz, which is four to five orders of magnitude lower than the absolute vibration levels in the low frequency (\sim Hz) region measured on the standard dilution refrigerators (“Hex std” and “Triton” in Ref. 27) and two orders of magnitude

lower than even those with vibration isolation option (“Hex UQT” in Ref. 27). This suggests that the common-mode suppression in this frequency range is effective. In contrast, a few peaks are observed between 100Hz and 1 kHz, attributed to the mechanical beam modes of the pillars between each temperature plate or resonance modes of the active damping system. Then starting from slightly less than 1 kHz, the spectra follow the $\mathcal{O}(f^{-2})$ dependence, as reported.²⁷ Eventually, they reach the detection limit of our interferometer setup at approximately $7 \text{ pmHz}^{-1/2}$, which turned out to be limited by the noise floor of the oscilloscope, $\sim 6 \text{ mV}_{\text{rms}}$. It would have been possible to reach an order of magnitude lower sensitivity, where the limit would be set by the noise equivalent power of the photodiode (PD).

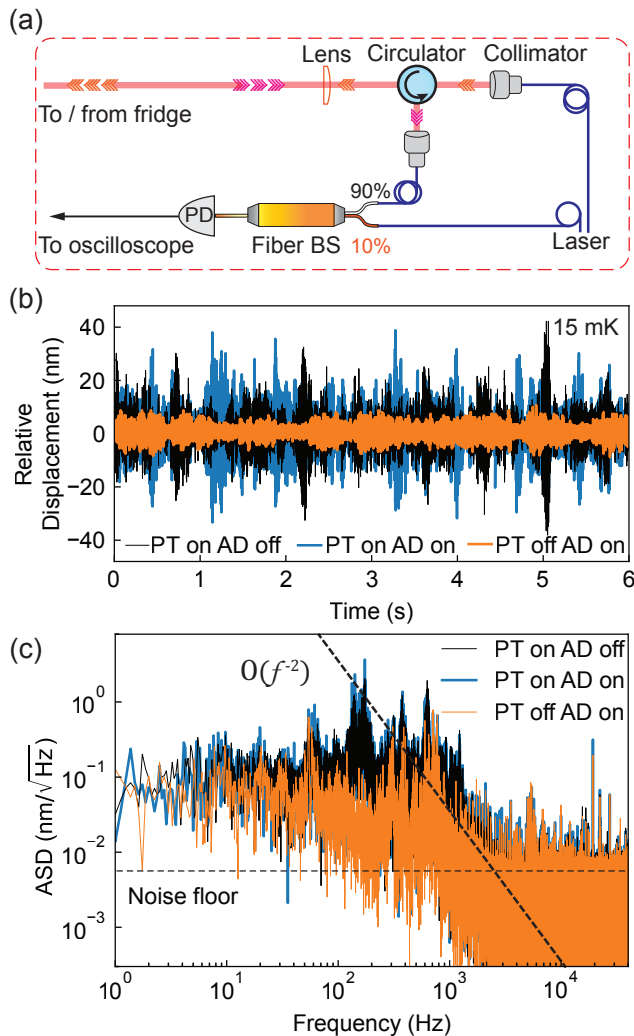


FIG. 2. Relative vibration measurement between the device on the MXC plate and the top optical breadboard. (a) Interferometer measurement setup. The reflected laser beam is directed to a fiber beam splitter (BS) through an optical circulator, combined with a local oscillator (LO), and detected by a photodiode (PD). (b) Relative displacement measurements at 15 mK, comparing PT off with AD on (orange), PT on with AD on (blue), and PT on with AD off (black). (c) Amplitude spectral density (ASD) derived from the fast Fourier transform (FFT) of the data in (b). The black dashed line represents the universal $\mathcal{O}(f^{-2})$ behavior (see main text).

III. RESULTS OF CAVITY STABILIZATION

A. Optical Cavity Device and Locking Setup

Figure 3 shows the design of the optical cavity device, which has two highly reflective mirrors. The top mirror is a concave highly reflective (HR) mirror with a reflectivity of $R \approx 99\%$ and radius of curvature 250 mm, attached to a piezo actuator (Piezomechanik, HPSt 150/14-10/12 with Black Coating). The piezo actuator enables *in-situ* cavity length tuning via applied voltage and is mounted on an invar ring to minimize mechanical contraction upon cooling. The bottom mirror is either a flat HR-coated mirror ($R \approx 99\%$) for the bare cavity or an HR-coated ($R \approx 99\%$) diamond crystal for the diamond-integrated cavity, as shown in Fig. 3(d).

The nominal distance between the two mirrors is designed to be approximately 30 mm, resulting in a free spectral range (FSR) of about 5 GHz. The mirror spacing can be globally adjusted using a cabinet with screw threads on its outer wall, which fits inside the enclosure housing, as shown in Fig. 3(b). This design enables tuning of the FSR from approximately 4.6 GHz to 6.5 GHz for the bare cavity and from 5.5 GHz to 9 GHz for the diamond-integrated cavity. The parameters for each cavity are summarized in Table I.

TABLE I. Summary of cavity parameters.

Parameter	Bare	Diamond-integrated
Cavity length (mm)	32.5	27.3
FSR (GHz)	4.6	5.5
Finesse, \mathcal{F}	310	90
Round trip loss (%)	2.00	6.75
Linewidth (MHz)	15	60
Quality factor, Q	2.7×10^7	6.5×10^6
Beam waist in radius (μm)	140	135
Mode Volume (mm^3)	0.50	0.39

We employed the Pound-Drever-Hall (PDH) method⁴⁸ to lock the resonance frequency of the cavity to the laser frequency, as depicted in Fig. 4. The ‘locking’ laser beam, phase-modulated at 150 MHz by a fiber electro-optic modulator (EOM), enters the cavity, and the reflected beam out of the fridge is routed through an optical circulator and detected by an avalanche photodiode (APD). The resulting electrical signals are mixed with the modulation signal to produce error signals, which are then processed by a digital PID circuit to generate a feedback signal. This feedback signal is amplified and directed back to the piezo actuator at the MXC stage to counteract the cavity displacement. Details of the setup are provided in the Appendix B 4. Notably, all the cavity locking results presented in the following sections are measured at PT on and AD on condition unless mentioned otherwise.

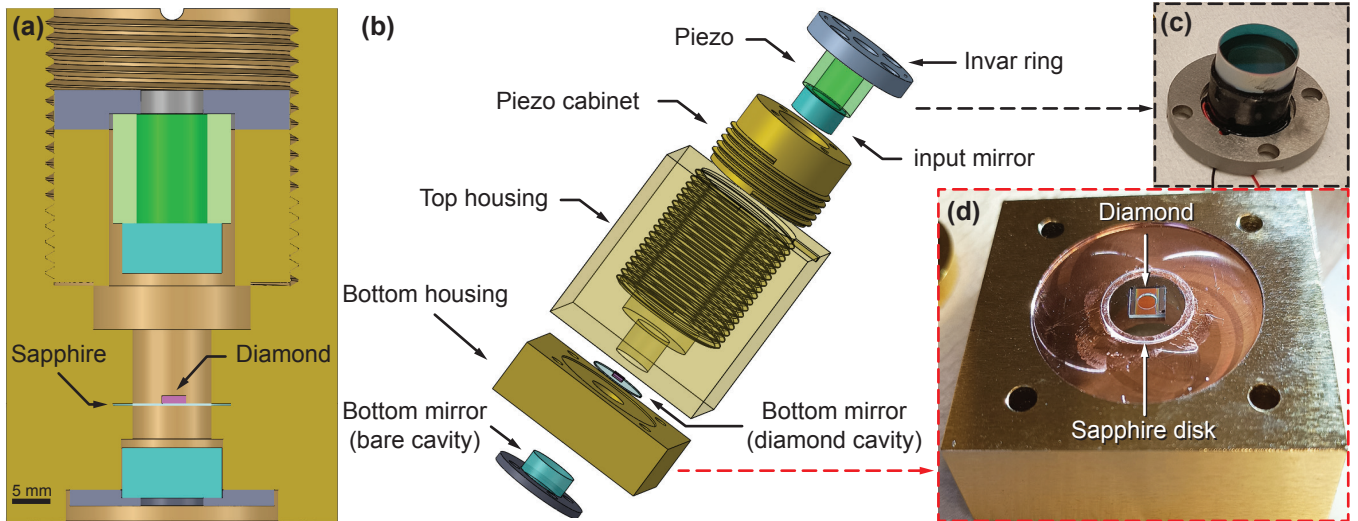


FIG. 3. Optical cavity device. (a) Cross-sectional view and (b) CAD rendering of the optical cavity housed in a gold-plated copper enclosure. The input mirror, an AR-HR coated mirror on a piezo actuator, is mounted on an invar ring [gray, photograph in (c)] and fixed to a threaded copper support for cavity length adjustment. The bottom mirror used for the ‘bare-cavity’ demonstration (Subsection III B) is also mounted on an invar ring and fixed to the bottom cavity housing. For the ‘diamond-integrated cavity’ demonstration (Subsection III C), the AR-HR coated diamond itself acts as the bottom mirror, mounted on a sapphire disk for thermalization and alignment using a small amount of vacuum grease [photograph in (d)]. Note that the bulk bottom mirror is unmounted in the ‘diamond-integrated cavity’.

B. Locking a Bare Cavity to a Laser

Using the setup, we stabilized a bare optical cavity—without the inclusion of diamond—at millikelvin temperature. To achieve stable locking of the cavity with a finesse \mathcal{F} , the root mean square (rms) of the cavity length fluctuation, δL_{rms} must be suppressed to:⁴⁹

$$\delta L_{\text{rms}} \leq \frac{\lambda}{2\mathcal{F}}, \quad (1)$$

where λ is the wavelength of the laser.

To identify the optical cavity spectrum, we initially scanned the cavity length by applying a triangular voltage to the piezo actuator. The transmitted signal amplitude and the error signal are represented by the blue and orange curves, respectively, on the right side of the top panel in Fig. 5(a). The two smaller sideband peaks in the blue curve originate from the phase modulation. From this and a wider scan (Fig. 12 in Appendix C 2), the finesse and FSR are estimated to be approximately 310 and 4.6 GHz, respectively.

The blue data plotted in Fig. 5(a) shows the transmission signal when the cavity is locked, maintaining near-maximum amplitude over several seconds. We further continued, and the lock was sustained for over an hour (Fig. 13 in Appendix C 2). The light orange curve represents the error signal, which was converted to cavity length displacement and plotted in the bottom panel. The root mean square (rms) of the cavity length fluctuation was determined to be approximately 30 pm, indicating that the setup can sustain an optical cavity with a finesse of approximately 1.2×10^4 at a wavelength of $\lambda = 737$ nm, as estimated from Eq. (1). The details of the analysis are provided in the Appendix C 2.

Note that the base temperature of our fridge, when the piezo actuator is shorted and the laser shutter is closed, is around 10 mK. When a static bias of around 75 V is applied to the

piezo actuator, the MXC temperature increases to 15 mK because of the static current flowing through parasitic resistance of the piezo actuator.

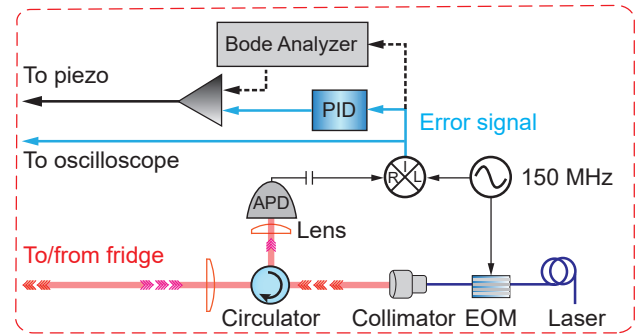


FIG. 4. PDH locking setup for the cavity. A frequency-stabilized laser is phase modulated by an electro optic modulator (EOM) and is directed into the fridge. Reflected light from the cavity is separated by an optical circulator and detected by an avalanche photodiode (APD). The detected signal generates an error signal through a mixer, fed into a digital PID controller, which provides feedback to the piezo actuator. The frequency response of the locked cavity is measured using a RedPitaya in Bode analyzer mode. All the optics are aligned on the fridge-top breadboard to maintain common-mode vibration.

C. Locking a Diamond-integrated Optical Cavity

Next, we investigated an optical cavity incorporating a 0.5 mm-thick bulk diamond crystal that is designed to develop a spin ensemble-based quantum transducer, as shown in Fig. 3 (d). However, bulk diamond crystals possess a high refractive index of 2.4 at the wavelength of 737 nm, which leads to significant Fresnel loss. To address this issue, previous studies

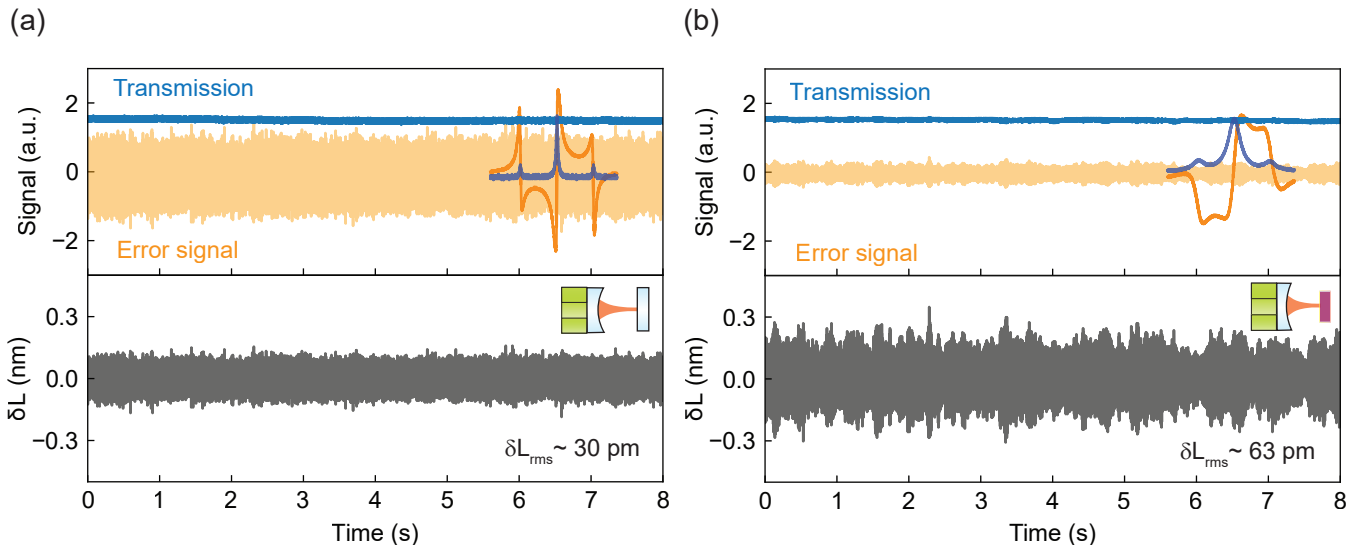


FIG. 5. Cavity stability measurement at 15 mK for (a) the bare cavity and (b) the diamond-integrated cavity. The upper panels show the scanning (dark) and locking (light) results for the error signal (orange) and transmitted signal (blue). The scanning plots are stretched along the x-axis. The bottom panels display the cavity length fluctuations derived from the error signals, with root mean square (rms) values of ≈ 30 pm for the bare cavity and ≈ 63 pm for the diamond-integrated cavity. The higher finesse of the bare cavity corresponds to better sensitivity, resulting in larger error signal amplitudes in (a) compared to (b).

have primarily focused on using thin diamond crystals, as thin as a few micrometers,^{50,51} or positioning a diamond crystal at the Brewster angle.⁵²

As an alternative to these approaches, we coated one side of the diamond with an anti-reflective (AR, $R < 0.25\%$) coating to mitigate the reflection,^{53–55} which appears better suited for the use of a bulk diamond crystal. The other side of the diamond was coated with a highly reflective (HR, $R \approx 99\%$) coating, serving as one mirror of the Fabry-Pérot cavity. Thanks to the AR coating, we did not observe ‘diamond-like’ or ‘air-like’ modes reported in cavities containing thin diamonds.^{50,51,56} Nevertheless, the birefringence of the diamond⁵⁷ caused a splitting of the transmitted signal, which we suppressed by adjusting the polarization using a half-wave plate mounted on top of the fridge.

Following the protocol used for the bare cavity, we obtained the cavity resonance peaks and subsequently locked the diamond-integrated cavity. The transmission and error signals, while the piezo was scanned, are displayed on the top right of Fig. 5(b). While well-separated and distinct sideband peaks are not observed for the diamond-integrated cavity due to its internal losses, the finesse and FSR could still be measured to be approximately 90 and 5.5GHz, respectively. The transmission and error signals under locking are indicated in Fig. 5(b) with light blue and light orange lines, respectively. The cavity length displacement during locking is plotted in the bottom panel of Fig. 5 (b), where the rms of the displacement is estimated to be ≈ 63 pm, indicating that the setup can lock the diamond-integrated cavity with a finesse of approximately 5.8×10^3 at a wavelength of $\lambda = 737$ nm from Eq. 1.

D. Origin of the Internal Loss in the Diamond-Integrated Cavity

The measured finesse of $\mathcal{F} \approx 90$ corresponds to a total cavity loss of $\approx 6.8\%$ per round trip, which exceeds the mirror transmission loss of 2% per round trip. To investigate the origin of the additional loss of 4.8% , we first considered surface scattering loss on the diamond. To this end, the roughness of the diamond surface was analyzed using atomic force microscopy before and after the optical coating, as elaborated in the Appendix B 1. The root mean square roughness was measured to be $R_q = 1.5$ nm, enabling us to estimate the total integrated scattering loss (S) using the relation:⁵⁸

$$S \approx \left(\frac{4\pi R_q}{\lambda/n} \right)^2, \quad (2)$$

where $n = 2.4$ is the refractive index of diamond. The loss per round trip due to the surface scattering is estimated to be $\approx 0.8\%$, leaving the majority of the total loss of approximately 4% unexplained. Clipping loss was also evaluated and found to be negligible, as the diameter of the beam waist $2w_0 \approx 270 \mu\text{m}$ is much smaller than the aperture of the dielectric coating on the diamond substrate, $D = 3$ mm. This results in a clipping loss of⁵⁹ $e^{-2(D/2w_0)^2} \approx 0$. Although an off-centered beam due to misalignment could theoretically cause clipping loss. However, the finesse of ≈ 90 reproduced over several cooldown cycles rules out this possibility.

Based on the estimated scattering and clipping losses, we conclude that the internal loss of 4% is most likely due to absorption inside the diamond, attributed to sub-bandgap defects.⁵⁷ The absorption loss in the current configuration is given by $1 - 10^{-2d\alpha}$, where α and d represent the absorption coefficient and the diamond thickness, respectively. From this, the absorption coefficient is estimated to be $\alpha \approx$

0.15 cm^{-1} , which aligns well with the results measured at a laser wavelength of approximately 737 nm for low nitrogen concentration diamond samples reported in Ref. 57. We note that this absorption loss could be mitigated by using diamonds with lower defect densities,⁵⁷ which would enable the realization of a higher finesse diamond-integrated cavity. Using a thinner diamond crystal would be another viable approach.

Lastly, we observed that the finesses of both the bare and diamond-integrated cavities remained nearly constant from room temperature to low temperatures, suggesting that the optical coatings on the bulk mirrors and diamond were minimally affected by temperature changes.

E. Cavity Length Fluctuation under Different Temperatures

Cavity length fluctuations, δL_{rms} , while locked may vary under different system temperatures. To assess this, we measured δL_{rms} for both cavities, the bare and diamond-integrated, at three different temperatures: room temperature (RT), 4 K, and 15 mK, with The results are summarized in Table II. The rms length fluctuation for the bare cavity remains approximately 30 pm (20 pm) during the PT on (PT off) conditions, as the device temperature varies from 4 K to millikelvin.

In contrast, the diamond-integrated cavity exhibits slight variations in δL_{rms} when the temperature changes from 4 K to 15 mK, for both PT on and off conditions. Also, the corresponding δL_{rms} value is significantly higher for the diamond-integrated cavity than the bare cavity when the PT is on. Currently, we attribute the larger fluctuation to the relatively weak clamping of the sapphire disk to the bottom housing, which will also be discussed in the next Subsection.

TABLE II. Comparison of root-mean-square (rms) cavity length fluctuations, δL_{rms} in picometers, for bare and diamond-integrated cavities at different temperatures. PT stands for pulse tube cooler.

δL_{rms} (pm)	Bare		Diamond-integrated	
	PT on	PT off	PT on	PT off
RT	-	23.5	-	13.1
4 K	31.6 ± 0.2	19.8	46.0 ± 0.7	21.5
15 mK	30 ± 3	19.9	63 ± 3.6	16.8

F. Mechanical Modes of the System

While the amplitude spectral density (ASD) of the relative vibrations, shown in Fig. 2(c) in Subsection II B, provides insights into the mechanical vibrations at the device, it lacks sensitivity in the higher frequency range from around 1 kHz, where the signal levels fall below the detection limit of our interferometer. In contrast, the length fluctuations δL in the cavity-locked configuration, plotted in the bottom panels of Figs. 5(a) and (b), also contain information about such mechanical vibrations. Moreover, one can expect to measure the spectrum over the bandwidth of the feedback PID circuit, $\sim 100\text{ kHz}$ thanks to the cavity. To address this, we plot the ASD of the bare and diamond-integrated cavities on the

top panels in Figs. 6 (a) and (b). Several clusters of peaks emerge in the frequency range from 100 Hz to $\sim 10\text{ kHz}$, as previously reported.²⁷⁻²⁹ We attribute these peaks to beam vibration modes of the fridge or resonance modes of the active damping system. Furthermore, vibration modes of the optical cavity device and its supporting thermalization tube may also contribute to these spectra, as many modes were identified in this frequency range in simulations (Appendix C 3).

Although three distinct peaks were observed at approximately 6 kHz, 11 kHz, and 20 kHz in the diamond-integrated cavity, only the 6 kHz peak has been reproduced across multiple cooldowns but slightly moving around each time. This suggests that these modes are associated with the bottom-mirror-coated diamond, which is manually placed on a sapphire disk with a tiny amount of vacuum grease applied to the edge. This likely introduces changes in the cavity arrangement during each cooldown.

Finally, the piezo actuator may also contribute to the observed modes in the ASD plot. To investigate this, we measured the frequency response of the cavity for both the bare and diamond-integrated cavities under locked conditions using a Bode analyzer, as shown in Fig. 4. A low-amplitude sinusoidal signal in the frequency range from 100 Hz to 40 kHz was generated by the analyzer and applied to the piezo actuator. The error signal was then fed into the analyzer, enabling it to acquire the frequency response of the locked cavity. The results are shown in the bottom panels in Figs. 6(a) and (b). Notably, unlike the ASD data, the Bode gain and phase data reveal several resonances only in the high-frequency region, especially around 6 kHz, 18 kHz, and 30 kHz for the bare cavity. For the diamond-integrated cavity, clusters of peaks centered around 6 kHz and 12 kHz were observed. Those peaks may arise from the mechanical resonances of the piezo actuator. Additionally, we note that the stycast adhesive between the piezo actuator and the invar ring may act as a spring, which could contribute to mechanical resonances in the $\sim \text{kHz}$ range at cryogenic temperatures.¹²

IV. CONCLUSION

We demonstrated the stabilization of Fabry-Pérot optical cavities, one bare and one diamond-integrated, at millikelvin temperatures in a custom cryogen-free dilution refrigerator. Mechanical vibrations were mitigated by placing an optical breadboard on top of the refrigerator, synchronizing the optical cavity device on the MXC plate with the fridge's absolute vibrations in a common mode. The incorporation of a bulk diamond crystal was achieved through the application of anti-reflective and highly reflective coatings. As a result, the cavity was locked to a free-running laser, a critical milestone towards a practical quantum transducer. Cavity length fluctuations of 30 pm and 63 pm were achieved for the bare and diamond-integrated cavities, respectively, corresponding to achievable finesses of 1.2×10^4 and 5.8×10^3 . The primary source of loss in the diamond-integrated cavity was identified as absorption, which could potentially be mitigated by using a diamond crystal with fewer defects.

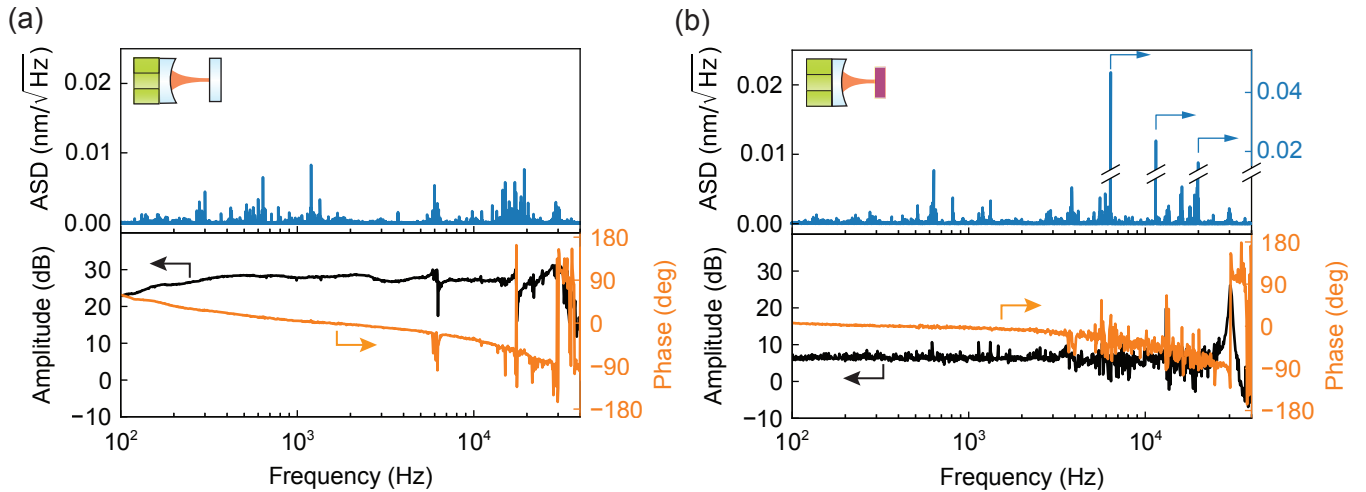


FIG. 6. Cavity response function measured while locking the cavity at 15 mK. Top panels: (a) and (b) show the amplitude spectral density (ASD) measured from the fast Fourier transform (FFT) of the cavity length fluctuations presented in the bottom panels of Fig. 5 for the bare and diamond-integrated cavities, respectively. Bottom panels: (a) and (b) display the transfer function (Bode plot) for the bare and diamond-integrated cavities, respectively. The measurements were performed by sending a low-amplitude sinusoidal signal at each frequency to the piezo actuator.

ACKNOWLEDGMENTS

The authors thank P. Burns and J. Kindem for generously sharing their expertise on the optical cryostat setup, and R. Yamazaki and A. Noguchi for the valuable insights into cryo-optical cavities. The authors also thank S. Uetake for sharing his expertise in fabricating and assembling the invar components, as well as the electronics for cavity-lock. Additionally, we are grateful to the members of the Hybrid Quantum Device Team within the Science and Technology Group and the Experimental Quantum Information Physics Unit at Okinawa Institute of Science and Technology Graduate University (OIST) for their insightful discussions. The authors also acknowledge for the help and support provided by the Engineering Section of Core Facilities at OIST. This work has been supported by the JST Moonshot R&D Program (Grant No. JPMJMS2066), JST-PRESTO (Grant No. JPMJPR15P7), Grant-in-Aid for JSPS Fellows (Grant No. 24KJ2178), The Nakajima Foundation, The Sumitomo Foundation, and OIST Graduate University.

AUTHOR DECLARATIONS

Conflict of Interest

The authors have no conflicts to disclose.

AUTHOR CONTRIBUTIONS

T.H. and A.B. equally contributed to this work. Y.K. conceived the principle of the project. T.H. initiated the experiments. A.B., T.H. and Y.K. designed the device, conducted the experiments, and analyzed the data. Y.K. and H.T. jointly supervised the project. All authors contributed to the

manuscript.

DATA AVAILABILITY STATEMENT

The data that support the findings of this study are available from the corresponding author upon reasonable request.

Appendix A: The Dilution Refrigerator Configuration

Here we provide detailed information about our dilution refrigerator setup that is designed to minimize the mechanical vibrations. In addition we introduce how to irradiate the laser from the top of the fridge to the device, which is anchored to the MXC stage.

1. Passive Stabilization

We implemented passive mitigation strategies to address three primary mechanical noise sources anticipated in our cryogen-free dilution refrigerator system (Bluefors, LD400). The first one is acoustic noise from the helium compressor for the pulse tube cooler, which can travel through the ground or air to the cryostat. To mitigate this, we placed the helium compressor in a separate ‘pump room’, approximately 4 meters away from the fridge, and installed a soundproof wall between the rooms to reduce the acoustic noise. The second source is mechanical vibration noise transmitted to the cryostat via metal vacuum pipes connected to the turbo pump used for helium mixture circulation. We suppressed this noise by installing ‘T-dampers’ at the top of the fridge and at the top of the turbo pump in the pump room. The final and seemingly largest source is the rotational motor valve of the pulse tube cooler. To mitigate this, the motor valve and buffer tanks are mechanically fixed and anchored to the building frame above the ceiling. Those countermeasures are illustrated in the photographs in Fig. 7.

The optical breadboard, a custom-made product based on FB-162126(Y) by HERZ Co., LTD, is fixed on top of a 70mm-thick aluminum plate. The main body of our dilution refrigerator is also supported by this aluminum plate, facilitating the common-mode vibration rejection. To accommodate these heavy components, whose total weight exceeds the maximum load capacity allowed for the frame used for a standard LD-400, we used a thicker aluminum frame designed for larger systems, such as the XLD series by Bluefors.

2. Active Stabilization

In addition to the passive countermeasures, we implemented ‘active’ mitigation to address vibrations from the ground, building structure, pedestrian traffic, and the rotational motor valve of the pulse tube cooler. An active damping system (Table Stable, AVI-400-M) was installed between the aluminum plate and the aluminum frame, as shown in Fig. 7. This system detects displacements and actively cancels them, within a frequency range of 1 Hz to 200 Hz, as demonstrated in Fig. 1(b) in the main text.

3. Optical Port Setup

To enable optical access into the dilution refrigerator, we installed optical windows on each temperature stage and at the bottom of their radiation shields, as shown in Fig. 8. Thermal radiation through the optical windows was minimized by reducing their diameter to less than 1.0 inch. We selected fused

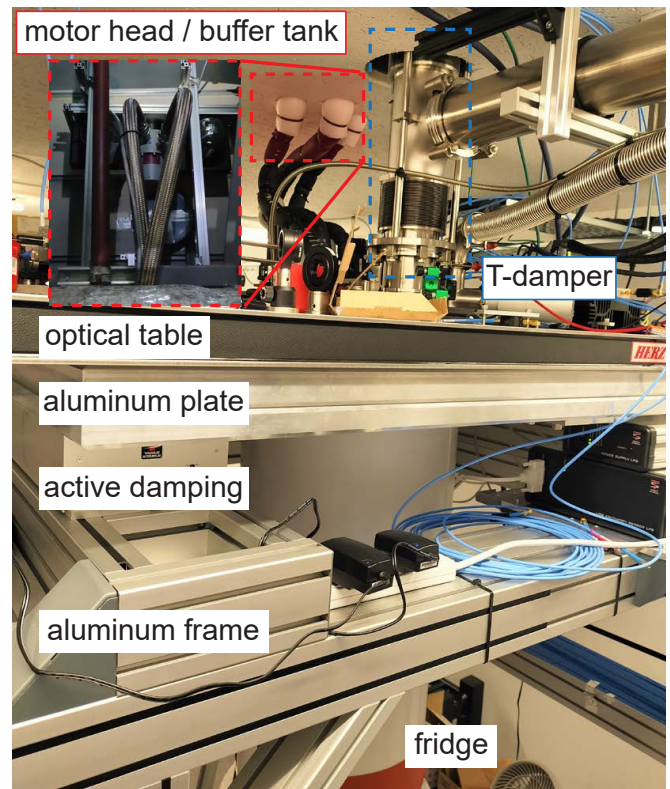


FIG. 7. The dilution refrigerator and implemented countermeasures for vibration mitigation. The photographs highlight key components, including the active damping system, T-dampers, and mechanical anchoring of the pulse tube cooler. See text for further details.

silica and BK-7 as the materials for the optical windows, as each blocks specific ranges of infrared light. To further reduce thermal radiation entering the fridge, narrow band-pass filter-coated windows were installed at the room temperature stage (vacuum-tight) and the 4 K stage. Anti-reflection (AR) coatings were applied to the windows at the other temperature stages to minimize reflective losses. All optical windows were mounted into custom-made ‘KF40 to SM1-threaded lens tube’ flange adapters made of SUS304 stainless steel, which were fixed to the central line-of-sight flanges on respective temperature plates. The optical windows on the radiation shields, located at the bottom in Fig. 8, were fixed by thin elastic metal plates.

Figure 8 illustrates the combination of optics for each stage. Due to the long distance between fridge-top optical table and the device, we installed two lenses ($f=500$ mm), one at room temperature and the other at the cold plate inside the fridge, to construct the 4f-relay system.

Appendix B: SAMPLE AND EXPERIMENTAL DETAILS

1. Samples

The diamond sample used in this experiment is a single crystal synthesized by the chemical vapor deposition (CVD) method sourced from Element Six Technologies. The crystal has dimensions of $4.5 \times 4.5 \times 0.5$ mm, with its surface aligned to the [001] crystallographic orientation. Substitutional nitro-

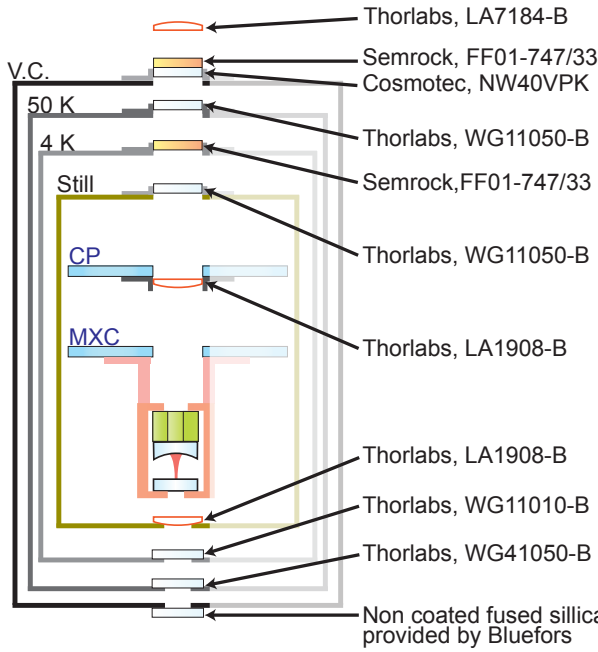


FIG. 8. The combination of the optics inside dilution refrigerator

gen impurities, known as P1 centers, are present at a concentration of less than 1 ppm. The presence of any other color centers, such as nitrogen-vacancy centers, is anticipated to be negligible.

The crystal underwent mechanical polishing (Syntek co., Ltd.) to remove any graphite layers, followed by cleaning in a boiling mixed-acid solution of HNO_3 , H_2SO_4 , and HClO_4 in a 1:1:1 volume ratio for 10 minutes at 200°C .⁶⁰ The acid treatment was performed within a fume hood, utilizing a setup similar to the one detailed in Ref. 60. One face of the diamond was coated with an anti-reflection coating ($R < 0.25\%$ @ 737 nm), while the opposite face was coated with a high-reflective coating ($R = 99 \pm 0.5\%$ @ 737 nm). Both optical coatings were applied using ion beam sputtering (IBS) at Sigmakoki Co., Ltd.

We evaluated the surface roughness of the diamond sample using an atomic force microscope (Bruker, Icon 3). As a measure of roughness, we estimate the root mean square deviation (R_q) after each sample treatment and the corresponding values are $R_q \approx 0.3\text{ nm}$ after mechanical polishing and $R_q \approx 1.5\text{ nm}$ after optical coating using IBS.

2. Cryogenic Piezo for Optical Cavity

The optical cavity, as elaborated in the main text, consists of two HR-coated mirrors, and the entire system is installed inside a gold-plated copper enclosure. We used Stycast (LOCTITE, 2850FTJ and CAT 23LVJ), an epoxy resin commonly used for cryogenic experiments, to fix the piezo actuator (Piezomechanik, HPS150/14-10/12 with Black Coating) and mirror to the invar ring plate. However, standard piezo actuators often cracked during the cooling cycles due to the mismatch in the coefficients of thermal expansion. This issue was resolved by using a piezo actuator (shown in Fig. 3 (c) in the main text), which is coated with a thin layer of Stycast

across its surface. The coating effectively mitigates stresses due to thermal contraction during the cooling.

3. Interferometer Experiment Setup

Figure 9 illustrates the interferometer setup for relative vibration measurements. A Ti:Sapphire laser (M-squared, SolisTiS), placed on a ground-based optical table referred to as the 'Floor setup' in Fig. 9, was tuned to approximately 737 nm and stabilized by locking it to an internal reference cavity. The stabilized laser beam was split into two, which were subsequently coupled into polarization-maintaining optical fibers [Fig. 9(a)]. On the fridge-top optical table, one of the collimated laser beams was directed to the cavity input mirror mounted on the MXC stage inside the dilution refrigerator [Fig. 9(b)]. The reflected signal was routed through an optical circulator and combined with the local oscillator (LO) laser beam at a fiber beam splitter ['Fiber BS' in Fig. 9 (b); Thorlabs, PN850R2A1]. The resulting interference was then detected by a photodiode (PD; Thorlabs, PDA36A-EC). The absolute laser wavelength was continuously monitored by a wavemeter (HighFinesse, WS7-60).

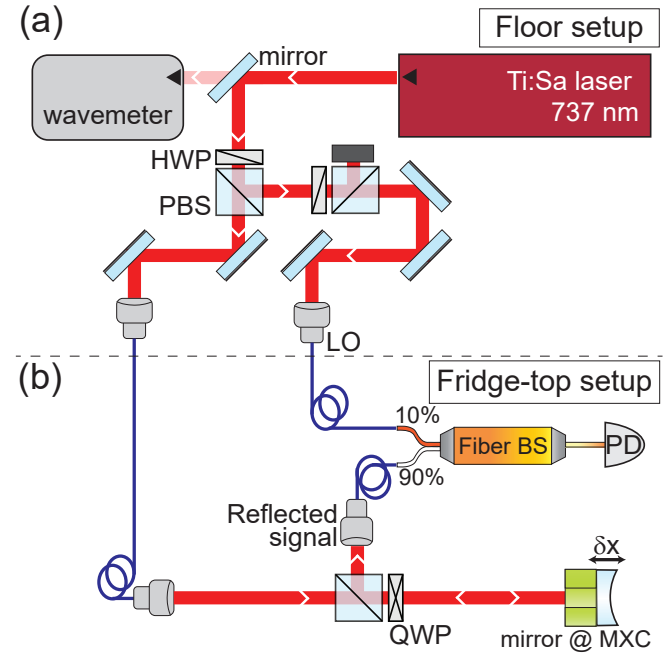


FIG. 9. Interferometer setup for relative vibration characterization. (a) Optical system on the ground-based optical table. A small portion of the laser beam is directed to a wavemeter for wavelength monitoring, while the remaining is split into two using tunable beamsplitters, consisting of a half-waveplate (HWP; CASIX, WPZ1417-L/2-737) and a polarization beamsplitter (PBS), and then coupled into polarization-maintaining optical fibers. (b) Optical system on the fridge-top optical breadboard. The collimated laser beam from one of the optical fibers is directed to the cavity input mirror inside the dilution refrigerator. The reflected laser beam is circulated by the combination of a quarter-waveplate (QWP; CASIX, WPZ1417-L/4-737) and PBS. This reflected signal and the local oscillator signal interfere at the fiber beamsplitter, and the resulting signal is detected by a photodiode (PD).

4. Cavity Locking Experiment Setup

We employed the standard PDH locking scheme to stabilize the cavity inside the dilution refrigerator. The experimental setup installed on top of the fridge is schematically illustrated in Fig. 4 of the main text. A frequency-stabilized laser (M-squared, Solstis) was phase-modulated at 150 MHz using a fiber-based electro-optic modulator (EOM; iXBlue, NIR-MPX800-LN-0.1). The modulated light was directed into the fridge via a series of mirrors and focused onto the optical cavity using a pair of lenses, each with a focal length of 500 mm, arranged in a 4f configuration. The light reflected from the cavity was detected using a high-speed avalanche photodiode (APD; Thorlabs, APD430A/M). The signal was passed through a bias tee (Mini-Circuits, ZFBT-4R2G-FT+) to separate the AC and DC components. The DC component was sent directly to an oscilloscope to monitor the reflected signal, while the AC component was filtered by a band-pass filter (Mini-Circuits, SBP-150+) and mixed with a reference signal from a signal generator using a frequency mixer (Mini-Circuits, ZLW-1-1+), producing the error signal. The error signal was then fed into a digital PID controller (TEM, Laselock), which generates a feedback signal. This feedback signal was amplified by a bipolar piezo driver (MESS-TEK Co., Ltd., M-2629) and sent to the piezo actuator to lock the cavity. Additionally, the frequency response of the piezo actuator during locking was measured using an FPGA-based RedPitaya (STEMlab 125-14) in the Bode analyzer module. The dotted lines in Fig. 4 indicate the connections to the RedPitaya.

Appendix C: DATA ANALYSIS

In this section, we detail the characterization process for the relative vibration and the cavity length fluctuation while locking the cavity.

1. Relative Vibration

Here, we detail the analysis and fitting methods used to determine the relative length fluctuations. The results in Fig. 2(b) were analyzed as follows: to estimate the relative displacement in units of length, we scanned the mirror by applying a periodic triangular voltage to the piezo actuator. The resulting reflection data were fitted with a sinusoidal function described by:

$$y = A \sin(2\pi ft + \phi) + D, \quad (\text{C1})$$

where, A is the amplitude, f the interfering oscillation frequency, ϕ is the phase, and D is the offset. The relative vibration signal, measured with the piezo actuator at zero applied voltage, was then converted into a length displacement (δx) using the following expression:

$$\delta x = \arcsin\left(\frac{y-D}{A}\right) \frac{\lambda}{4\pi}, \quad (\text{C2})$$

where λ is the wavelength of the excitation laser. In Fig. 10(a), the scan and relative vibration data are shown as solid

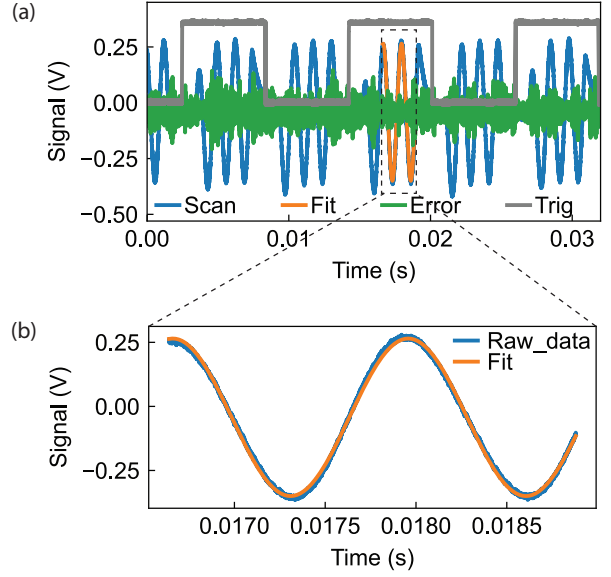


FIG. 10. Analysis of relative vibration results. (a) Time-dependent scan and relative vibration signals are shown in solid blue and green colors, respectively. A portion of the scan data is fitted with a sin function to determine the relative length fluctuation of the fridge. (b) A zoomed-in view of the sinusoidal fitting function is shown.

blue and solid green curves, respectively, while the solid orange line represents the sinusoidal fitting using Eq. C1. A zoomed-in view of the fitting function is shown in Fig. 10(b) for clarity. As shown in Fig. 2(b) in the main text, the peak-to-peak length fluctuations (δL_{p-p}) are estimated to be ≈ 60 nm when the PT is on, and ≈ 10 nm when the PT is off. Moreover, we measured the relative displacement and the corresponding ASD spectral response estimated at 4K, as shown in Figs. 11 (a) and (b), respectively. As mentioned in the main text, we hardly notice any significant difference between the ASD spectral response measured at 15 mK and 4K. Therefore, we infer that the turbo pump operating at 820 Hz, used for Helium circulation, has minimal impacts on the displacement measurements.

2. Cavity Length Fluctuation

Here, we detail the methods used to estimate cavity fluctuations in length. In Fig. 12(a), we present the cavity transmission obtained by scanning the bare cavity's length over a wide range to measure the free spectral range (FSR). The incoming laser is modulated at 150 MHz using an electro-optic-modulator (EOM) to generate sidebands. The TEM₀₀ Gaussian modes and sidebands were fitted with sets of three Lorentzian functions each to determine the FSR value and the finesse (\mathcal{F}) of the cavity. The FSR (finesse) value for the bare cavity is approximately 4.6 GHz ($\mathcal{F} = 310$), while for the diamond cavity, it is around 5.5 GHz ($\mathcal{F} = 90$). In Fig. 12(b), the error and transmitted signals for the bare cavity during scanning are shown. We fitted the transmission spectrum with Lorentzian functions (orange solid line). Additionally, the slope of the error signal, highlighted by the blue dashed box, is plotted separately on the right side of the main plot

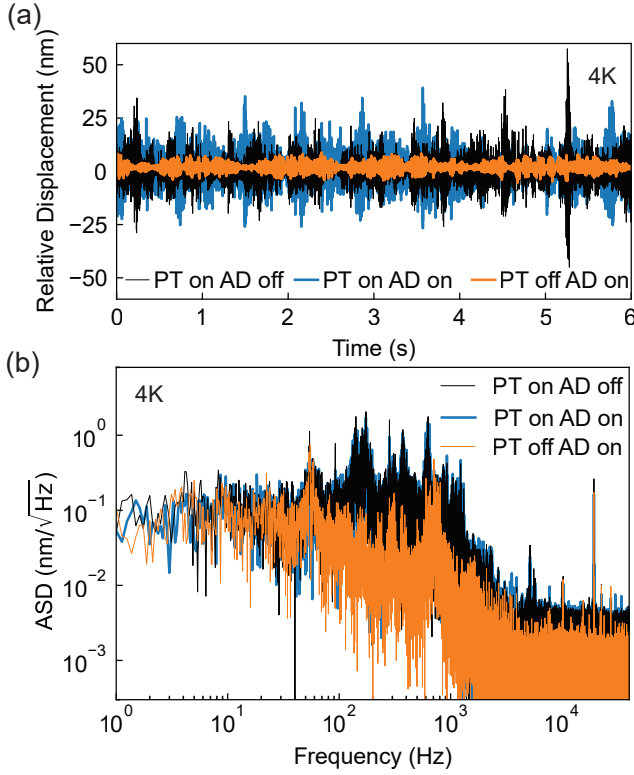


FIG. 11. Relative vibration results measured at 4K. (a) Relative displacement measurements are shown for three different conditions: PT on AD off, PT on AD on and PT off AD on. (b) Amplitude spectral density (ASD) measured from the displacement data show similar spectral behavior as measured at 15 mK temperatures, shown in the main text Fig. 2(c).

and fitted with a hyperbolic tangent function (black solid line). These fittings allow us to convert the error signal to the cavity length displacement using the cavity linewidth in length (ΔL), which follows the relation

$$\Delta L = \frac{\lambda}{2\mathcal{F}} \quad (\text{C3})$$

where λ is the laser wavelength. With the finesse and the laser wavelength known, we converted the cavity linewidth from time to length unit. Finally, the error signal in voltage was converted into length fluctuations by analytically applying the inverse function of the hyperbolic tangent, as shown in the right panel of Fig. 12(b):

$$y = \frac{1}{2} \log \left(\frac{1+x}{1-x} \right), \quad (-1 < x < 1) \quad (\text{C4})$$

In the main article, we demonstrate cavity locking over a short duration. However, the cavity can remain locked even for hours without requiring re-locking. Here, in Fig. 13, the cavity stability is measured over a period exceeding one hour. The locked data remain stable throughout the measurement, with the observed fluctuations attributed to a drift in laser power. This result indicates the stability and robustness of the cavity locking.

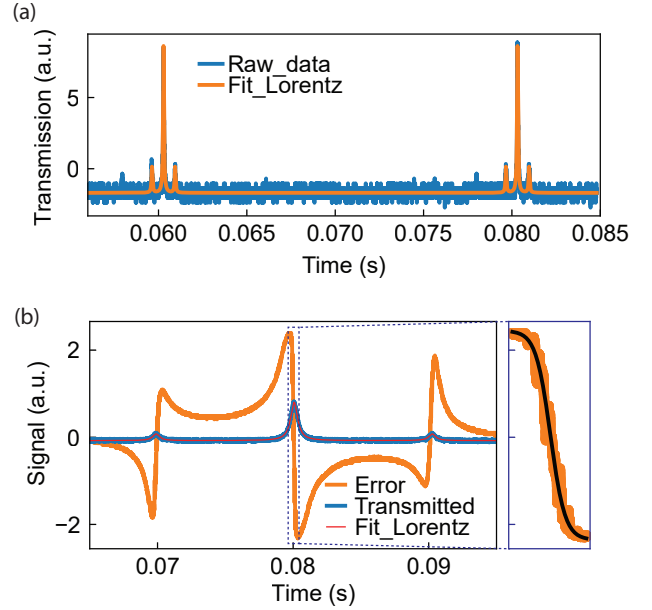


FIG. 12. Analysis of the cavity scanning spectra. (a) A wide scan data produces the FSR value of the bare cavity in the transmission mode. The modes and the corresponding sidebands are fitted with three Lorentzian functions (solid orange line) to estimate the FSR and finesse value. (b) Transmitted and error signals are shown for the bare cavity. The slope of the error signal (encircled with a blue dashed line) is plotted separately and fitted with the hyperbolic tangent function (solid black line). The fitting enables to evaluate the conversion factor more precisely.

3. Mechanical Modes of the Cavity

We performed numerical simulations to estimate the mechanical modes of the optical cavity device assembly using the Solid Mechanics module of COMSOL Multiphysics software. The simulation model replicated the real cavity structure, as shown in the left part of Fig. 14. A long cylindrical copper thermalization tube (height ≈ 280 mm) was included, extending from the bottom of the MXC plate to position the sample at the center of the external magnetic field. We used the fixed constraint boundary condition across the physical joints to estimate the mechanical modes. The simulations were performed in the eigenfrequency modes, revealing mechanical modes ranging from a few kHz to tens of kHz. An example of a simulated mechanical mode is displayed on the right-hand side of Fig. 14, showing a mode around 8 kHz. This mode is close to the intense peak around 6 kHz, observed in both bare and diamond-integrated cavities, shown in Fig. 6(b). However, the simulations could not reproduce the exact frequencies observed experimentally. This discrepancy is likely due to unknown parameters such as the spring constant of the vacuum grease at cryogenic temperatures, the precise amount of grease used, and the geometric complexity of the device.

- ¹J. A. Boyd and T. Lahaye, *American Journal of Physics* **92**, 50 (2024).
- ²M. Aspelmeyer, T. J. Kippenberg, and F. Marquardt, *Reviews of Modern Physics* **86**, 1391 (2014).
- ³H. Mabuchi, *Science* **298**, 1372 (2002).
- ⁴H. Walther, B. T. H. Varcoe, B.-G. Englert, and T. Becker, *Reports on Progress in Physics* **69**, 1325 (2006).
- ⁵A. Reiserer and G. Rempe, *Reviews of Modern Physics* **87**, 1379 (2015).

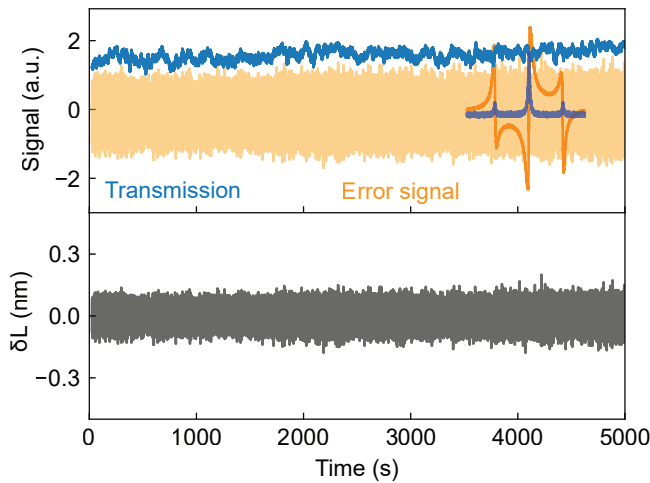


FIG. 13. Stability of the bare cavity measured over an extended duration of time while locked at millikelvin temperature. The upper panel shows the scanning (dark) and locking (light) data for the error (orange) and transmitted (blue) signals. A representative scan is presented for reference on the right, with the horizontal axis not to scale. The bottom panel shows the cavity length fluctuation in unit of nm derived from the locked error signal.

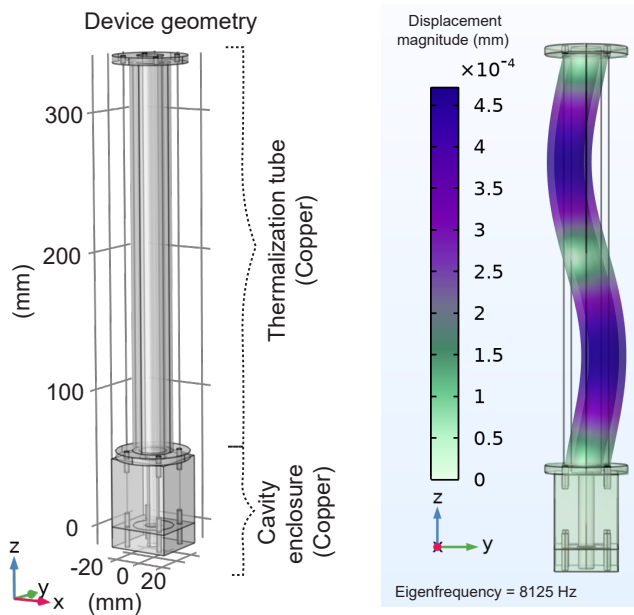


FIG. 14. Mechanical modes of the device using COMSOL Multiphysics simulation. The schematic design in the left side displays the device geometry including the big copper thermalization tube. Right side image shows the mechanical mode of the whole system appearing around 8 kHz

⁶A. Reiserer, *Reviews of Modern Physics* **94**, 041003 (2022), publisher: American Physical Society.
⁷P. Lodahl, S. Mahmoodian, and S. Stobbe, *Reviews of Modern Physics* **87**, 347 (2015).
⁸P. Senellart, G. Solomon, and A. White, *Nature Nanotechnology* **12**, 1026 (2017), publisher: Nature Publishing Group.
⁹O. Wipfli, H. F. Passagem, C. Fischer, M. Grau, and J. P. Home, *Review of Scientific Instruments* **94**, 083204 (2023).

¹⁰H. Zhong, G. Fläschner, A. Schwarz, R. Wiesendanger, P. Christoph, T. Wagner, A. Bick, C. Staarmann, B. Abeln, K. Sengstock, and C. Becker, *Review of Scientific Instruments* **88**, 023115 (2017).
¹¹T. Ruelle, D. Jaeger, F. Fogliano, F. Braakman, and M. Poggio, *Review of Scientific Instruments* **93**, 095003 (2022).
¹²A. Kumar, A. Suleymanzade, M. Stone, L. Taneja, A. Anferov, D. I. Schuster, and J. Simon, *Nature* **615**, 614 (2023), publisher: Nature Publishing Group.
¹³T. Akutsu and f. t. K. collaboration), *Journal of Physics: Conference Series* **610**, 012016 (2015), publisher: IOP Publishing.
¹⁴K. Stannigel, P. Rabl, A. S. Sørensen, P. Zoller, and M. D. Lukin, *Physical Review Letters* **105**, 220501 (2010).
¹⁵P. Rabl, S. J. Kolkowitz, F. H. L. Koppens, J. G. E. Harris, P. Zoller, and M. D. Lukin, *Nature Physics* **6**, 602 (2010).
¹⁶M. Tsang, *Physical Review A* **81**, 063837 (2010).
¹⁷A. H. Safavi-Naeini and O. Painter, *New Journal of Physics* **13**, 013017 (2011).
¹⁸Y.-D. Wang and A. A. Clerk, *Physical Review Letters* **108**, 153603 (2012), publisher: American Physical Society.
¹⁹R. Hisatomi, A. Osada, Y. Tabuchi, T. Ishikawa, A. Noguchi, R. Yamazaki, K. Usami, and Y. Nakamura, *Physical Review B* **93**, 174427 (2016).
²⁰C. Javerzac-Galy, K. Plekhanov, N. R. Bernier, L. D. Toth, A. K. Feofanov, and T. J. Kippenberg, *Physical Review A* **94**, 053815 (2016).
²¹C. Zhong, Z. Wang, C. Zou, M. Zhang, X. Han, W. Fu, M. Xu, S. Shankar, M. H. Devoret, H. X. Tang, and L. Jiang, *Physical Review Letters* **124**, 010511 (2020).
²²L. A. Williamson, Y.-H. Chen, and J. J. Longdell, *Physical Review Letters* **113**, 203601 (2014), text.ids= williamsonMagnetoOpticModulatorUnit2014a publisher: American Physical Society.
²³P. S. Barnett and J. J. Longdell, *Physical Review A* **102**, 063718 (2020), text.ids= barnettTheoryMicrowaveopticalConversion2020a, barnettTheoryMicrowaveopticalConversion2020b publisher: American Physical Society.
²⁴S. Wehner, D. Elkouss, and R. Hanson, *Science* **362**, eaam9288 (2018), publisher: American Association for the Advancement of Science.
²⁵M. Ruf, N. H. Wan, H. Choi, D. Englund, and R. Hanson, *Journal of Applied Physics* **130**, 070901 (2021).
²⁶D. Awschalom, K. K. Berggren, H. Bernien, S. Bhave, L. D. Carr, P. Davids, S. E. Economou, D. Englund, A. Faraon, M. Fejer, S. Guha, M. V. Gustafsson, E. Hu, L. Jiang, J. Kim, B. Korzh, P. Kumar, P. G. Kwiat, M. Lončar, M. D. Lukin, D. A. Miller, C. Monroe, S. W. Nam, P. Narang, J. S. Orcutt, M. G. Raymer, A. H. Safavi-Naeini, M. Spiropulu, K. Srinivasan, S. Sun, J. Vučković, E. Waks, R. Walsworth, A. M. Weiner, and Z. Zhang, *PRX Quantum* **2**, 017002 (2021).
²⁷E. Olivieri, J. Billard, M. De Jesus, A. Juillard, and A. Leder, *Nuclear Instruments and Methods in Physics Research Section A: Accelerators, Spectrometers, Detectors and Associated Equipment* **858**, 73 (2017).
²⁸D. Schmoranzler, A. Luck, E. Collin, and A. Fefferman, *Cryogenics* **98**, 102 (2019).
²⁹A. Chijioko and J. Lawall, *Cryogenics* **50**, 266 (2010).
³⁰Mohammad Mirhosseini, A. Sipahigil, M. Kalaei, and O. Painter, *Nature* **588**, 599 (2020), number: 7839 Publisher: Nature Publishing Group.
³¹Y. Xu, A. A. Sayem, L. Fan, C.-L. Zou, S. Wang, R. Cheng, W. Fu, L. Yang, M. Xu, and H. X. Tang, *Nature Communications* **12**, 4453 (2021), number: 1 Publisher: Nature Publishing Group.
³²W. Hease, A. Rueda, R. Sahu, M. Wulf, G. Arnold, H. G. Schwefel, and J. M. Fink, *PRX Quantum* **1**, 020315 (2020), publisher: American Physical Society.
³³M. J. Weaver, P. Duivesteyn, A. C. Bernasconi, S. Scharmer, M. Lemang, T. C. v. Thiel, F. Hijazi, B. Hensen, S. Gröblacher, and R. Stockill, *Nature Nanotechnology* **19**, 166 (2024), publisher: Nature Publishing Group.
³⁴J. Rochman, T. Xie, J. G. Bartholomew, K. C. Schwab, and A. Faraon, *Nature Communications* **14**, 1153 (2023), number: 1 Publisher: Nature Publishing Group.
³⁵K.-M. C. Fu, G. Z. Iwata, A. Wickenbrock, and D. Budker, *AVS Quantum Science* **2**, 044702 (2020).
³⁶N. Aslam, H. Zhou, E. K. Urbach, M. J. Turner, R. L. Walsworth, M. D. Lukin, and H. Park, *Nature Reviews Physics* **5**, 157 (2023), publisher: Nature Publishing Group.
³⁷Y. Kubo, C. Grezes, A. Dewes, T. Umeda, J. Isoya, H. Sumiya, N. Morishita, H. Abe, S. Onoda, T. Ohshima, V. Jacques, A. Dréau, J.-F. Roch, I. Diniz, A. Auffeves, D. Vion, D. Esteve, and P. Bertet, *Physical Review Letters* **107**, 220501 (2011).

- ³⁸X. Zhu, S. Saito, A. Kemp, K. Kakuyanagi, S.-i. Karimoto, H. Nakano, W. J. Munro, Y. Tokura, M. S. Everitt, K. Nemoto, M. Kasu, N. Mizuochi, and K. Semba, *Nature* **478**, 221 (2011).
- ³⁹C. Grezes, B. Julsgaard, Y. Kubo, M. Stern, T. Umeda, J. Isoya, H. Sumiya, H. Abe, S. Onoda, T. Ohshima, V. Jacques, J. Esteve, D. Vion, D. Esteve, K. Mølmer, and P. Bertet, *Physical Review X* **4**, 021049 (2014).
- ⁴⁰A. Sipahigil, R. E. Evans, D. D. Sukachev, M. J. Burek, J. Borregaard, M. K. Bhaskar, C. T. Nguyen, J. L. Pacheco, H. A. Atikian, C. Meuwly, R. M. Camacho, F. Jelezko, E. Bielejec, H. Park, M. Lončar, and M. D. Lukin, *Science* **354**, 847 (2016).
- ⁴¹T. Iwasaki, F. Ishibashi, Y. Miyamoto, Y. Doi, S. Kobayashi, T. Miyazaki, K. Tahara, K. D. Jahnke, L. J. Rogers, B. Naydenov, F. Jelezko, S. Yamasaki, S. Nagamachi, T. Inubushi, N. Mizuochi, and M. Hatano, *Scientific Reports* **5**, 12882 (2015).
- ⁴²T. Iwasaki, Y. Miyamoto, T. Taniguchi, P. Siyushev, M. H. Metsch, F. Jelezko, and M. Hatano, *Physical Review Letters* **119**, 253601 (2017).
- ⁴³X. Fernandez-Gonzalvo, S. P. Horvath, Y.-H. Chen, and J. J. Longdell, *Physical Review A* **100**, 033807 (2019), `tex.ids= fernandez-gonzalvoCavityenhancedRamanHeterodyne2019a` publisher: American Physical Society.
- ⁴⁴G. G. King, P. S. Barnett, J. G. Bartholomew, A. Faraon, and J. J. Longdell, *Physical Review B* **103**, 214305 (2021), `tex.ids= kingProbingStrongCoupling2021a`, `kingProbingStrongCoupling2021b` publisher: American Physical Society.
- ⁴⁵S. Blum, C. O'Brien, N. Lauk, P. Bushev, M. Fleischhauer, and G. Morigi, *Physical Review A* **91**, 033834 (2015).
- ⁴⁶B. Li, P.-B. Li, Y. Zhou, S.-L. Ma, and F.-L. Li, *Physical Review A* **96**, 032342 (2017), publisher: American Physical Society.
- ⁴⁷C. O'Brien, N. Lauk, S. Blum, G. Morigi, and M. Fleischhauer, *Physical Review Letters* **113**, 063603 (2014).
- ⁴⁸E. D. Black, *American Journal of Physics* **69**, 79 (2000).
- ⁴⁹S. Vadia, J. Scherzer, H. Thierschmann, C. Schäfermeier, C. Dal Savio, T. Taniguchi, K. Watanabe, D. Hunger, K. Karraï, and A. Högele, *PRX Quantum* **2**, 040318 (2021), publisher: American Physical Society.
- ⁵⁰E. Janitz, M. Ruf, M. Dimock, A. Bourassa, J. Sankey, and L. Childress, *Physical Review A* **92**, 043844 (2015), publisher: American Physical Society.
- ⁵¹S. Raman Nair, L. J. Rogers, X. Vidal, R. P. Roberts, H. Abe, T. Ohshima, T. Yatsui, A. D. Greentree, J. Jeske, and T. Volz, *Nanophotonics* **9**, 4505 (2020).
- ⁵²A. Savvin, A. Dormidonov, E. Smetanina, V. Mitrokhin, E. Lipatov, D. Genin, S. Potanin, A. Yelissev, and V. Vins, *Nature Communications* **12**, 7118 (2021), number: 1 Publisher: Nature Publishing Group.
- ⁵³S. B. v. Dam, M. Ruf, and R. Hanson, *New Journal of Physics* **20**, 115004 (2018), publisher: IOP Publishing.
- ⁵⁴L. Xu, J. Zhang, G. Bian, P. Fan, M. Li, Y. Liu, N. Zhang, and H. Yuan, *AIP Advances* **10**, 085124 (2020).
- ⁵⁵T. K. Yeung, D. Le Sage, L. M. Pham, P. L. Stanwix, and R. L. Walsworth, *Applied Physics Letters* **100**, 251111 (2012).
- ⁵⁶S. Bogdanović, S. B. van Dam, C. Bonato, L. C. Coenen, A.-M. J. Zwerver, B. Hensen, M. S. Z. Liddy, T. Fink, A. Reiserer, M. Lončar, and R. Hanson, *Applied Physics Letters* **110**, 171103 (2017).
- ⁵⁷T. Luo, F. A. Hahl, J. Langer, V. Cimalla, L. Lindner, X. Vidal, M. Haertelt, R. Blinder, S. Onoda, T. Ohshima, and J. Jeske, *Philosophical Transactions of the Royal Society A: Mathematical, Physical and Engineering Sciences* **382**, 20220314 (2023), publisher: Royal Society.
- ⁵⁸J. M. Bennett, *Measurement Science and Technology* **3**, 1119 (1992).
- ⁵⁹D. Hunger, T. Steinmetz, Y. Colombe, C. Deutsch, T. W. Hänsch, and J. Reichel, *New Journal of Physics* **12**, 065038 (2010).
- ⁶⁰K. J. Brown, E. Chartier, E. M. Sweet, D. A. Hopper, and L. C. Bassett, *Journal of Chemical Health & Safety* **26**, 40 (2019), publisher: American Chemical Society.